



Nitridation Br-doped $\text{Li}_4\text{Ti}_5\text{O}_{12}$ anode for high rate lithium ion batteries

Jiaqing Wang^a, Zhenzhong Yang^b, Weihan Li^a, Xiongwu Zhong^a, Lin Gu^b, Yan Yu^{a,*}

^a CAS Key Laboratory of Materials for Energy Conversion, Department of Materials Science and Engineering, University of Science and Technology of China, Hefei, Anhui 230026, China

^b Beijing Laboratory for Electron Microscopy Institute of Physics, CAS, Beijing 100190, China

HIGHLIGHTS

- Br doping $\text{Li}_4\text{Ti}_5\text{O}_{12}$ powder was synthesized by solid state reaction.
- TiN layer formed on the surface of $\text{Li}_4\text{Ti}_5\text{O}_{11.7}\text{Br}_{0.3}$ powder after heating in NH_3 .
- The TiN coated $\text{Li}_4\text{Ti}_5\text{O}_{11.7}\text{Br}_{0.3}$ shows superior electrochemical performance.

ARTICLE INFO

Article history:

Received 21 January 2014

Received in revised form

8 May 2014

Accepted 12 May 2014

Available online 20 May 2014

Keywords:

Li-ion battery

Anode

$\text{Li}_4\text{Ti}_5\text{O}_{12}$

Nitridation

ABSTRACT

Br-doping $\text{Li}_4\text{Ti}_5\text{O}_{12}$ ($\text{Li}_4\text{Ti}_5\text{O}_{11.7}\text{Br}_{0.3}$) is fabricated by conventional solid state method and shows enhanced cycling performance compared with pristine $\text{Li}_4\text{Ti}_5\text{O}_{12}$. After thermal nitridation for 90 min in NH_3 , the $\text{Li}_4\text{Ti}_5\text{O}_{11.7}\text{Br}_{0.3}$ electrode exhibits better rate capability and excellent cycling performance. It delivers a reversible capacity of 138 mAh g^{-1} and 104 mAh g^{-1} after 100 cycles at 10C and 20C, respectively, which is approximately four and seven times higher than those of pristine $\text{Li}_4\text{Ti}_5\text{O}_{12}$ at the same current rates. This work indicates the feasibility of improving cycling performance and rate capabilities of $\text{Li}_4\text{Ti}_5\text{O}_{12}$ through controlling both surface termination and bulk doping procedures.

© 2014 Elsevier B.V. All rights reserved.

1. Introduction

Recently, the global environmental problems have attracted much attention which is mainly caused by scarce energy source. Li-ion batteries (LIBs) have been widely used for many portable electric devices such as cell phones, laptop computers and hybrid electric vehicles due to their high power, high energy density, and long cycle life. However, the current LIBs are handicapped by several critical disadvantages for large-scale application including low power density, short cycling life and especially safety hazards. The Li-insertion potential of carbonaceous materials is close to 0 V (vs. Li/Li^+), resulting in the dendritic lithium easily growing on the surface of anode during over-charge processes [1–7]. Therefore, alternative anode materials with higher Li insertion potential, better safety and excellent rate capability for the next generation of LIBs have been intensively investigated.

Spinel-type $\text{Li}_4\text{Ti}_5\text{O}_{12}$ (LTO) is an alternative anode material for LIBs due to the following advantages. First, it is a “zero-strain” material, which can undergo two-phase reaction and accommodate the structure change during lithium insertion and extraction processes, resulting in an excellent reversibility [8–14]. Second, it has a flat and a higher lithium insertion/extraction voltage at about 1.55 V (vs. Li/Li^+), thus the formation of SEI layers and electroplating of lithium are avoided [9,15]. Finally, Ti is an abundant element, allowing it to be a cost-effective material [9,15].

Despite the evident advantages, no anode material is flawless. The rate capability of LTO is relatively low because of its poor electronic conductivity (only $10^{-13} \text{ S cm}^{-1}$) and moderate Li^+ diffusion coefficient (10^{-14} – $10^{-17} \text{ cm}^2 \text{ s}^{-1}$) [9,15–17]. To date, many research efforts have been focused on overcoming these drawbacks, which include reducing the size of particles [6,18–22] or preparing nanostructured LTO anode with various morphologies (such as hollow or porous structure) [22–24]. Another approach to achieve enhanced electrochemical performance is to enhance the electronic conductivity by doping the spinel with metal or nonmetal ions [25–31] or by surface modification using conductive

* Corresponding author.

E-mail address: yanyumse@ustc.edu.cn (Y. Yu).

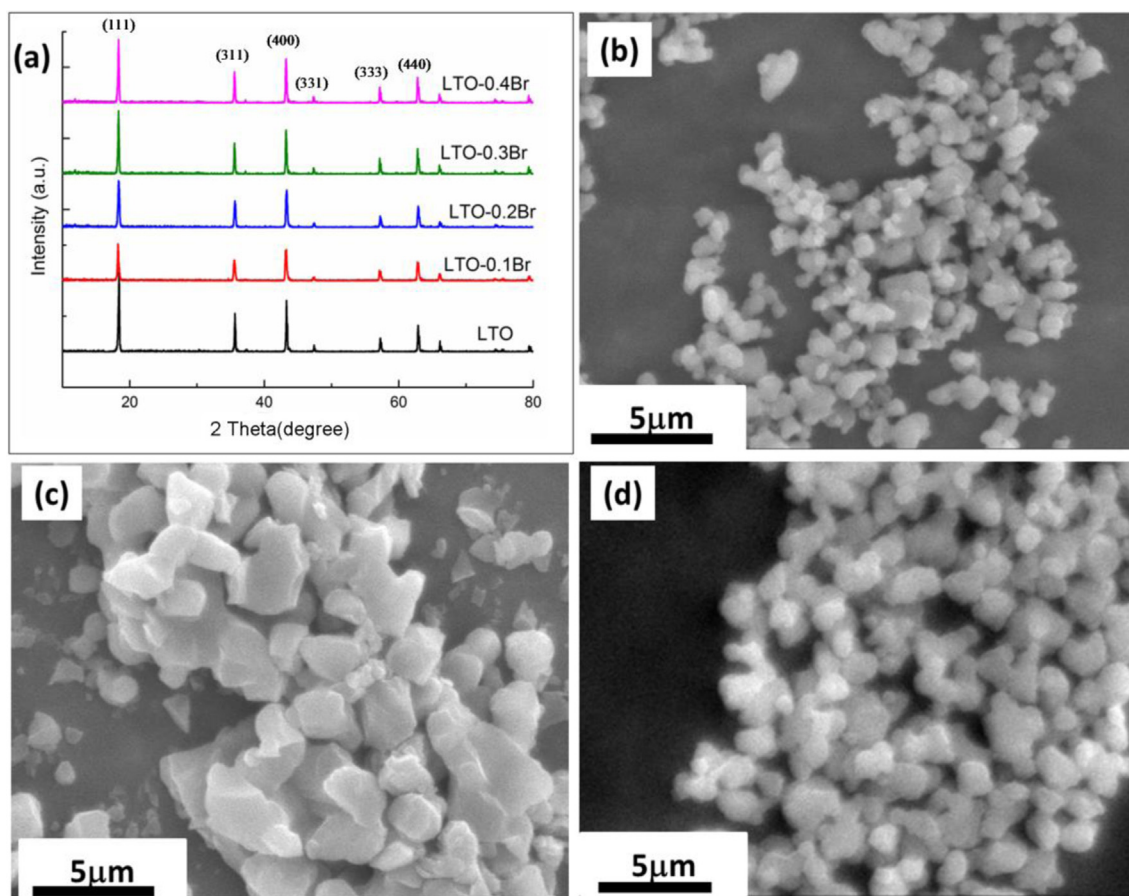


Fig. 1. (a) XRD patterns of synthesized LTO–xBr ($x = 0, 0.1, 0.2, 0.3, 0.4$). (b)–(d) SEM images of LTO powder calcinated at 800 °C (b), 900 °C (c), and LTO–0.3Br 800 °C (d), respectively.

coating species [32–37]. Qi et al. reported that LTO delivered an improved cyclability by doping nonmetal Br ion [29]. However, this Br-doped LTO anode presents a very limited improvement on the rate performance. Recently, it has been demonstrated that LTO with electronically conductive coating layers on the surface is the most effective way to enhance the conductivity. It shortens transport

lengths of both lithium ions and electrons and protecting the electrode from direct contact with the electrolyte, resulting in an enhanced rate capability of the battery [1,38].

Here, we improve both the cyclability and rate capability by thermal nitridation with an appropriate Br-doping level, $\text{Li}_4\text{Ti}_5\text{O}_{12-x}\text{Br}_x$ ($x = 0.3$) (denoted as LTO–0.3Br) anode. Benefiting from Br-doping and the improved electronic conductivity, the LTO–0.3Br anode shows better electrochemical performance in terms of specific capacity, cycling and rate performance than pure LTO. Furthermore, the LTO–0.3Br terminated with surface nitridation exhibits much improved rate capability compared with pristine LTO–0.3Br. This work indicates the feasibility of improving electronically conductive of LTO through both surface termination and bulk doping procedures.

Table 1

The lattice parameter of LTO–xBr ($x = 0, 0.1, 0.2, 0.3, 0.4$).

Sample	Lattice parameter (Å)
$\text{Li}_4\text{Ti}_5\text{O}_{12}$	8.3584
$\text{Li}_4\text{Ti}_5\text{O}_{11.9}\text{Br}_{0.1}$	8.3608
$\text{Li}_4\text{Ti}_5\text{O}_{11.8}\text{Br}_{0.2}$	8.3620
$\text{Li}_4\text{Ti}_5\text{O}_{11.7}\text{Br}_{0.3}$	8.3623

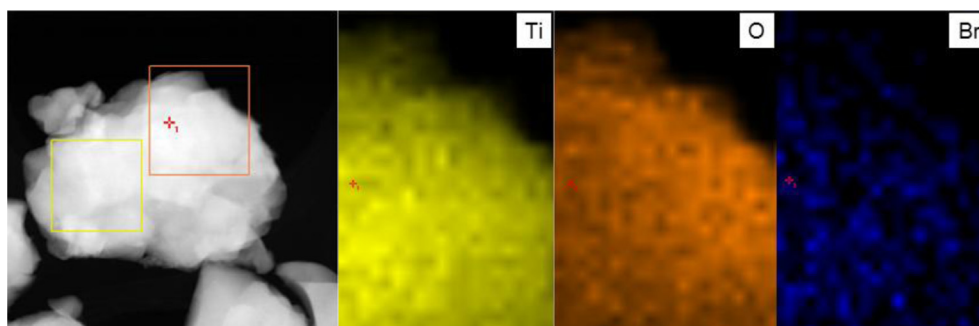


Fig. 2. The EDX mapping images and spectrum of LTO–0.3Br particles.

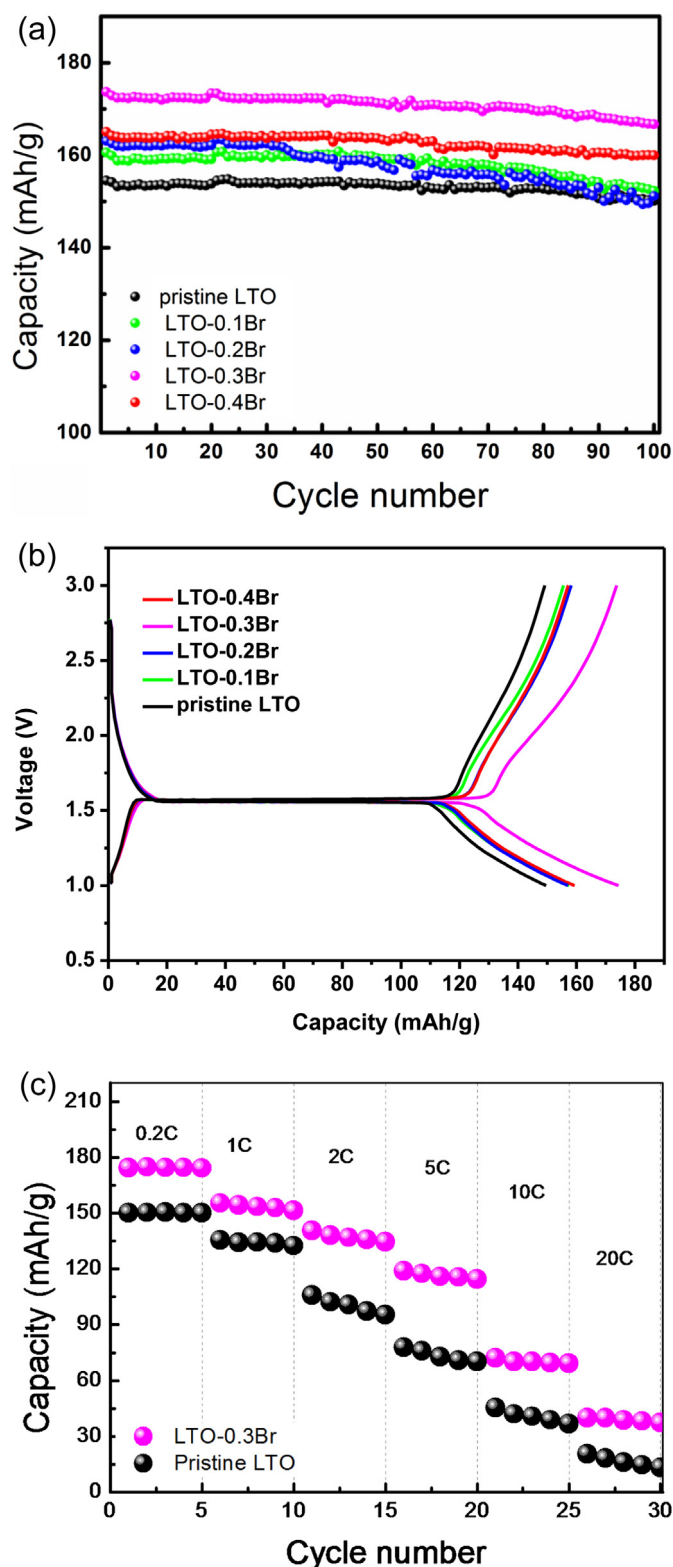


Fig. 3. (a) The cycling performances of LTO- x Br ($x = 0, 0.1, 0.2, 0.3, 0.4$) at 0.2C; (b) The voltage profiles of LTO- x Br ($x = 0, 0.1, 0.2, 0.3, 0.4$) at a rate of 0.2C; and (c) the rate and cycling performance of LTO and LTO-0.3Br at different C rate. The rate is marked in the picture.

2. Experimental

2.1. Synthesis of the $\text{Li}_4\text{Ti}_5\text{O}_{12}$ with and without Br-doping

$\text{Li}_4\text{Ti}_5\text{O}_{12-x}\text{Br}_x$ ($x = 0, 0.1, 0.2, 0.3, 0.4$) powders were prepared by conventional high temperature solid state reaction using $\text{LiOH} \cdot \text{H}_2\text{O}$, TiO_2 (amorphous) and $\text{LiBr} \cdot \text{H}_2\text{O}$ in a Li:Ti molar ratio of 4.35:5. All the reagents were bought from Sinopharm Chemical Reagent Co. Ltd, China. Excess Li was applied since Lithia may lose at high temperature during the process of synthesis. All the reagents were mixed in an agate mortar and ground for 1 h. Then the mixture was heated to 800 °C and 900 °C from room temperature. The temperature was maintained for 12 h in a muffle furnace, followed by natural cooling to room temperature.

2.2. Preparation of nitrated $\text{Li}_4\text{Ti}_5\text{O}_{11.7}\text{Br}_{0.3}$

The as-prepared powders LTO-0.3Br were heated from room temperature to 700 °C at the rate of 5 °C min^{-1} under Ar atmosphere. Then, the gas was changed into NH_3 and the temperature was kept at 700 °C for 30, 90 and 150 min, respectively, followed by natural cooling to room temperature under flowing Ar gas. The furnace was kept air-tight to prevent oxidation.

2.3. Characterization

The microstructural properties and phase composition of the synthesized powders have been studied by X-ray diffraction (XRD, Philips X'pert Pro Super), scanning electron microscopy (SEM, JEOL JSM-6390LA) and High-resolution transmission electronic microscopy (HR-TEM, JEOL 4000EX). Energy-dispersive X-ray spectroscopy (EDX) analysis was carried out by using an EDAX system (EDAX, Mahwah, NJ, USA) attached to a Zeiss SESAM (Carl Zeiss, Oberkochen, Germany) microscope operating at 200 keV. X-ray photoelectron spectroscopy (XPS) measurements and analyses were carried with an ESCALab220I-XL system.

2.4. Electrochemical characterization

The working electrode consisted of active material ($\text{Li}_4\text{Ti}_5\text{O}_{12-x}\text{Br}_x$ ($x = 0, 0.1, 0.2, 0.3, 0.4$) or nitrated LTO-0.3Br),

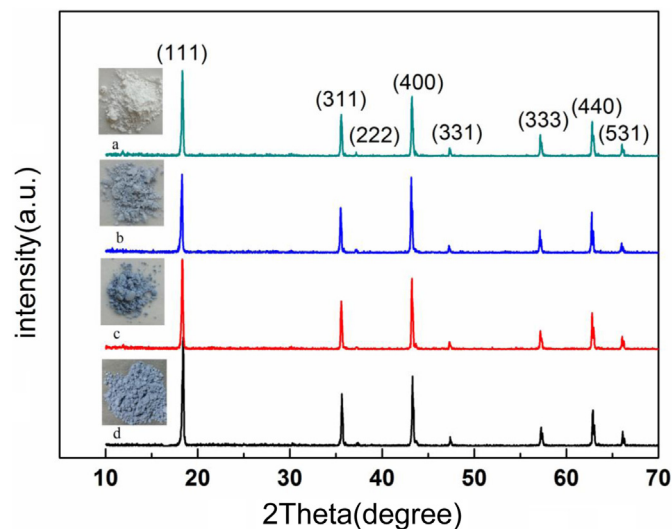


Fig. 4. XRD patterns of LTO-0.3Br with nitridation for different time. The inset pictures exhibit LTO-0.3Br powder color change after thermal nitridation at 700 °C with NH_3 gas flow.

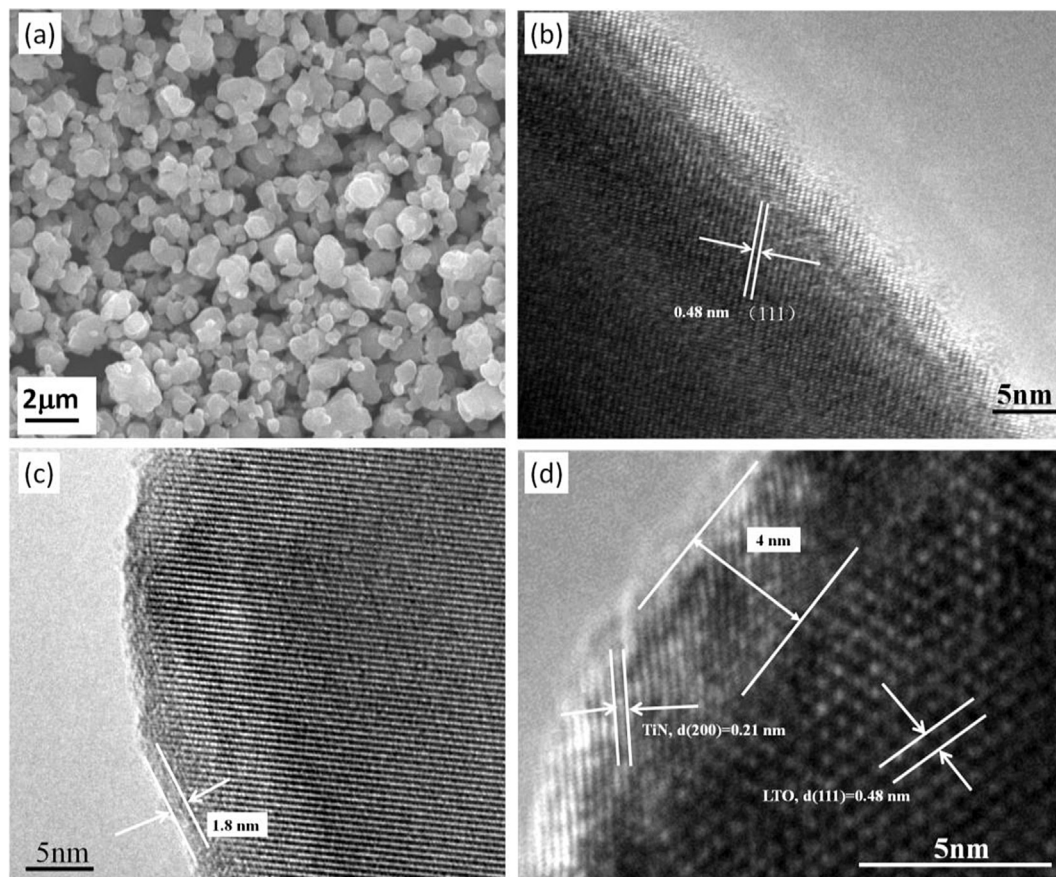


Fig. 5. (a) SEM image of LTO–0.3Br–N-90. HR-TEM images (b) pristine LTO–0.3Br, (c) LTO–0.3Br–N-30, (d) LTO–0.3Br–N-90 with TiN layer.

carbon black (Acetylene black), and PVDF (poly vinylidene fluoride) in a weight ratio of 80:10:10. The mixture was uniformly cast onto a pure copper foil and dried under vacuum at 80 °C overnight. Every cell was assembled in an argon-filled glove box (MBRAUN LABMASTER 130) where both moisture and oxygen levels were kept below 1 ppm with active material of about 5 mg in every cell. Pure lithium foil was used as both the counter electrode and reference electrode. The electrolyte was composed of 1.0 M LiPF_6 in a 50:50 (v/v) mixture of ethylene carbonate (EC) and diethyl carbonate (DEC). Celgard 2400 was used as the separator. Electrochemical measurements were conducted using two-electrode coin cells (2032) at room temperature, which were cycled in the voltage range between 3.0 V and 1.0 V (vs. Li^+/Li) with a NEWARE battery test system. The impedance spectra of the cells were carried out with the CHI 660d in the frequency range from 0.01 Hz to 100 kHz with the AC amplitude of 5.0 mV. The measurements were conducted at discharging state of 50% of the capacity.

2.5. Conductivity measurements

The conductivity measurements were measured by impedance spectroscopy using High Resolution Dielectric Analyzer (Novocontrol) in the frequency range of 10^7 – 10^{-2} Hz. The electronic conductivity was tested by polarization experiment using an ion blocking cell. For the ion blocking cell (Ti/LTO/Ti), Ti metal films were evaporated onto both sides of sample discs with a thickness of about 500 nm.

3. Results and discussion

Fig. 1a shows the XRD patterns of the synthesized LTO samples with and without Br-doping prepared by solid-state reaction. When Br-doping amount ranges from 0 to 0.4, the sharp reflections at 18.4, 30.2, 35.6, 37.1, 43.3, 47.4, 57.2, 62.8, 66.1, 74.3, 75.4, 79.4 and 82.3 (2θ) can be indexed to the spinel LTO phase with Fd-3m space group (JCPDS No. 49-0207). The color of the LTO powders with dopant Br kept white. No impurity peaks were detected, indicating that the dopant Br had entered the lattice structure of LTO without changing the structural characteristics. However, the lattice parameters increased with the increasing dopant as shown in Table 1 due to the larger radius of Br ion.

Fig. 1b and c show the SEM images of LTO calcinated at 800 °C and 900 °C, respectively. The samples exhibit block-shaped particles with a narrow particle size distribution. The particle size is 1–2 μm (Fig. 1b). While annealed at 900 °C, the diameter increases to about 2–3 μm (Fig. 1c). These results indicate that crystalline grain increase with the improvement of calcination temperature. SEM image of LTO–0.3Br calcinated at 800 °C is similar with the pristine LTO and exhibits a block-shaped particle with a diameter of 1–2 μm (Fig. 1d). From the EDX mapping images of the elements Ti, Br, O in Fig. 2, it could be observed that the distribution of Br elements is consistent with that of Ti and O, indicating that Br distribute uniformly in the LTO–0.3Br particles.

Fig. 3a shows the cycling performance of electrode using the synthesized LTO samples doped with various amount of Br calcinated at 800 °C as electrode. The pristine LTO delivered the lowest

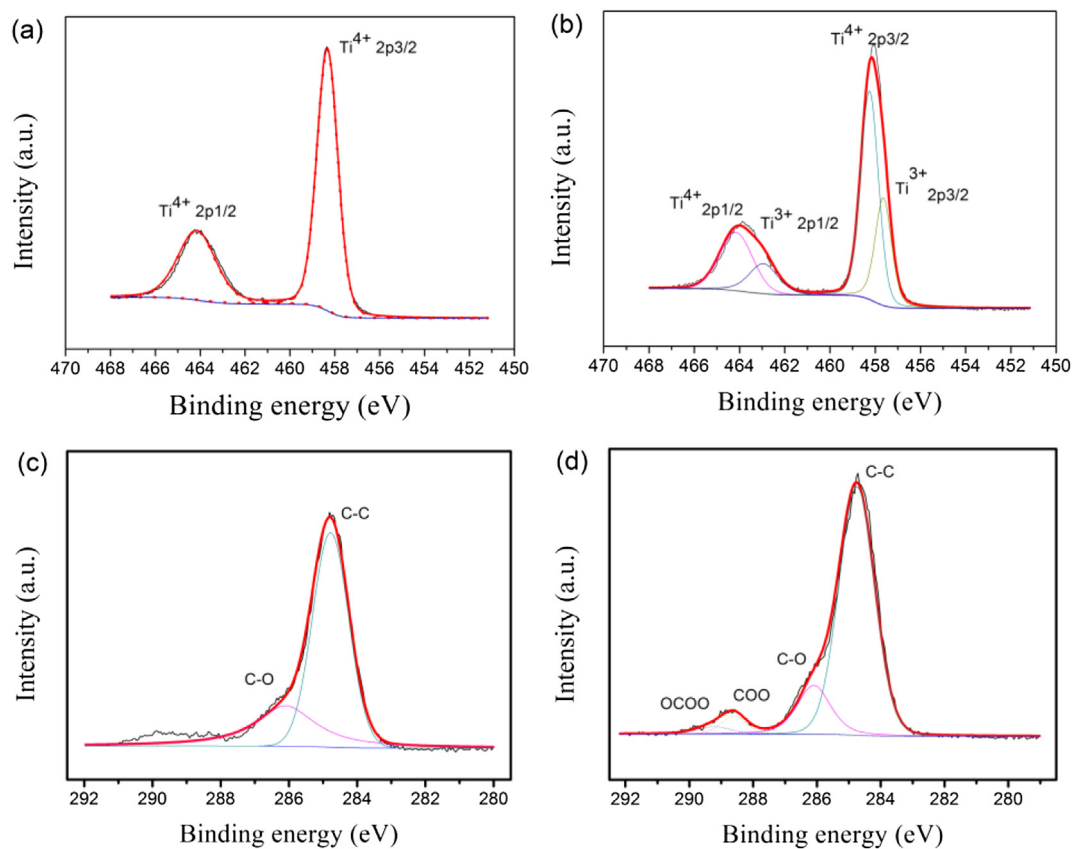


Fig. 6. XPS spectra (a) Ti2p in LTO–0.3Br, (b) Ti2p in LTO–0.3Br–N-90, (c) C1s in LTO–0.3Br and (d) C1s in LTO–0.3Br–N-90, respectively.

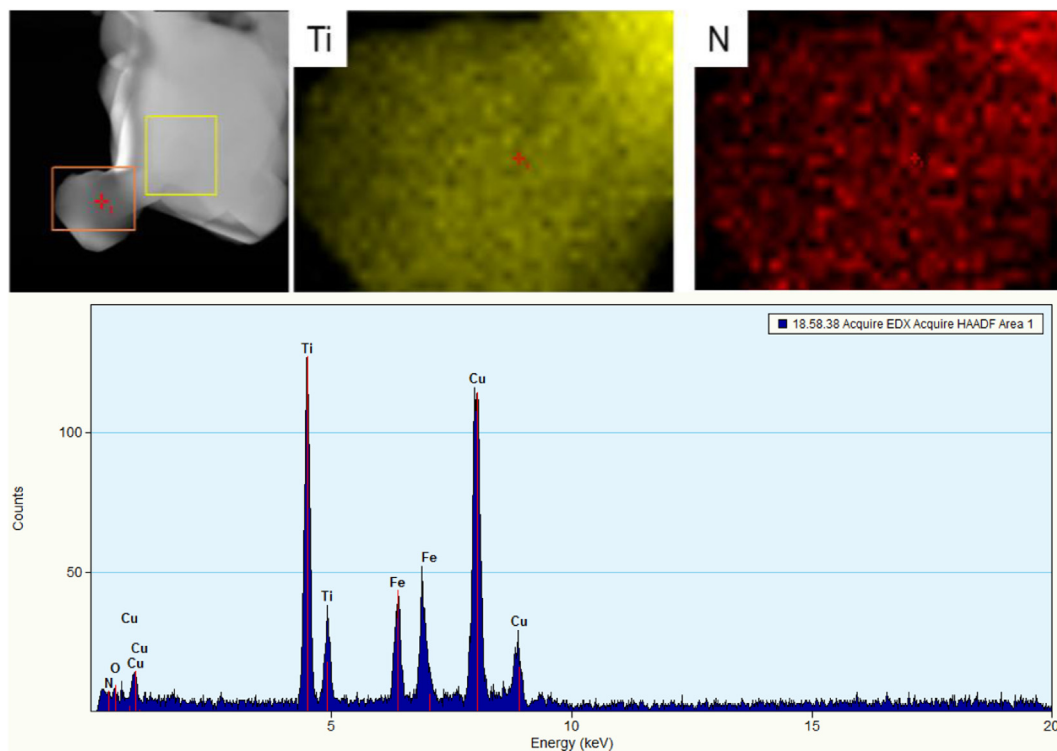


Fig. 7. EDX mapping images and spectrum of LTO–0.3Br–N-90. Here, the presence of elements Cu and Fe in the spectrum result from the specimen holder (Cu mesh) in transmission electronic microscopy.

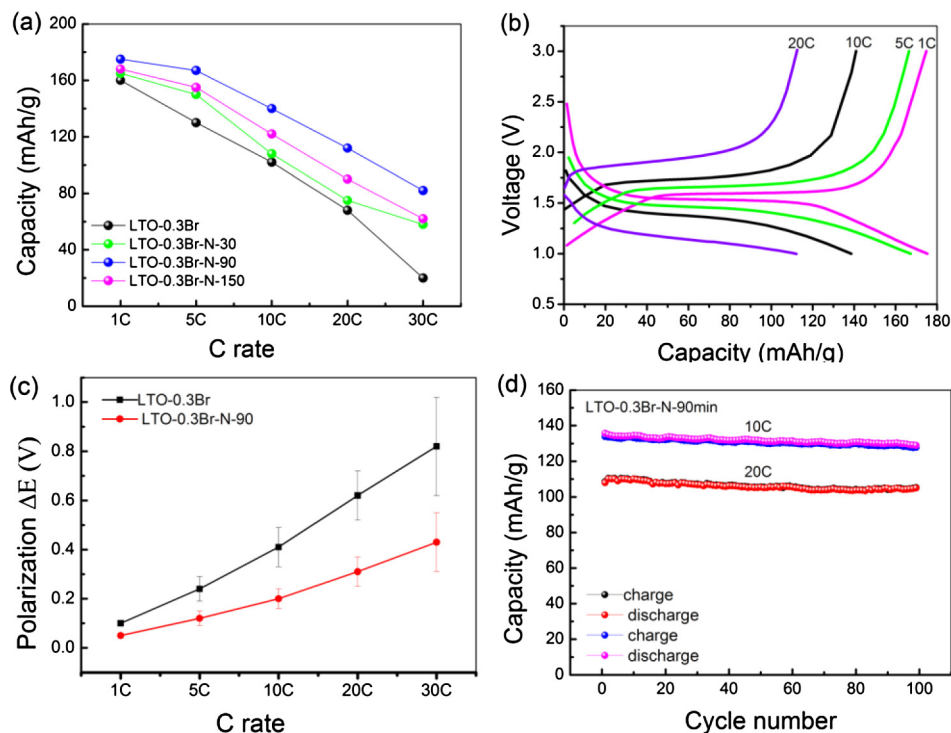


Fig. 8. (a) The rate capabilities of LTO–0.3Br–N-30, LTO–0.3Br–N-90 and LTO–0.3Br–N-150 compared with LTO–0.3Br; (b) The charge–discharge voltage profiles of LTO–0.3Br–N-90 at different C-rates (from 1C to 20C); (c) plots of ΔE of LTO–0.3Br and LTO–0.3Br–N-90 versus C rates; (d) cycling performance of LTO–0.3Br–N-90 at 10C and 20C.

reversible capacity (ca. 150 mAh g^{-1}) at 0.2C. The specific discharge capacity improved with increasing within the doping range of Br^- between 0 and 0.3. The discharge capacity of LTO–0.3Br reached about 165 mAh g^{-1} even after 100 cycles at 0.2C. Nevertheless, the capacity of the sample LTO–0.4Br fell back to 155 mAh g^{-1} because of doping too much Br^- in O^{2-} site and thus the increasing polarization [29,39].

Fig. 3b shows the voltage profiles of $\text{Li}_4\text{Ti}_5\text{O}_{12-x}\text{Br}_x$ ($x = 0, 0.1, 0.2, 0.3, 0.4$) at the current rate of 0.2C over a potential window of 1.0–3.0 V. All samples had a flat voltage plateau at the potential of 1.55 V, corresponding to the two phase coexistence between $\text{Li}_4\text{Ti}_5\text{O}_{12}$ and $\text{Li}_7\text{Ti}_5\text{O}_{12}$ [1]. The sloping voltage curves at the beginning/end of the discharge curves indicates a single phase insertion of $\text{Li}_{4+\delta}\text{Ti}_5\text{O}_{12}/\text{Li}_{7-\gamma}\text{Ti}_5\text{O}_{12}$ [7].

To get further evidence of the improvement of electrochemical performance of Br-doped LTO, the rate performance of LTO–0.3Br and pristine LTO samples were compared (Fig. 3c). The discharge capacities of the pristine LTO decreased significantly with the increasing current from 1C to 20C, whereas the LTO–0.3Br decreases much more slowly at the same rate. The LTO–0.3Br delivered capacities of 174, 152, 136, 115, 69, and 38 mAh g^{-1} at 0.2C, 1C, 2C, 5C, 10C and 20C, respectively. While in case of pristine LTO, it only delivers a capacity of 150, 139, 102, 75, 40, and 15 mAh g^{-1} at 0.2C, 1C, 2C, 5C, 10C, and 20C, respectively. The rate capabilities improvement of LTO–0.3Br indicates that appropriate amount of Br-doping decreases the polarization of LTO–0.3Br at various current density, compared to the pristine LTO [29]. The reversible capacity of LTO–0.3Br decreases very fast when the current density increase to 10C and 20C, respectively. It indicates that the internal resistance of the Br-doped samples does not significantly reduce.

In order to improve the rate capability of LTO–0.3Br, Thermal nitridation was applied for various time (denoted as LTO–0.3Br–N-30, LTO–0.3Br–N-90, and LTO–0.3Br–N-150, respectively). The samples with various time of nitridation showed identical XRD

patterns of LTO spinel phase (Fig. 4), indicating that the process of thermal nitridation doesn't change its phase in the core region. The inset images of Fig. 4 show the color change of LTO–0.3Br after nitridation. The white LTO–0.3Br powders turned into blue after thermal nitridation for 30 min and got darker with increasing time of nitridation. The color of the powders seemed no change when annealing in NH_3 longer than 90 min.

Fig. 5a shows SEM image of LTO–0.3Br–N-90. It can be seen clearly that the LTO–0.3Br–N-90 presented similar morphology and particle size with LTO–0.3Br. Fig. 5b shows the typical HRTEM image of LTO–0.3Br sample before nitridation. The intersecting

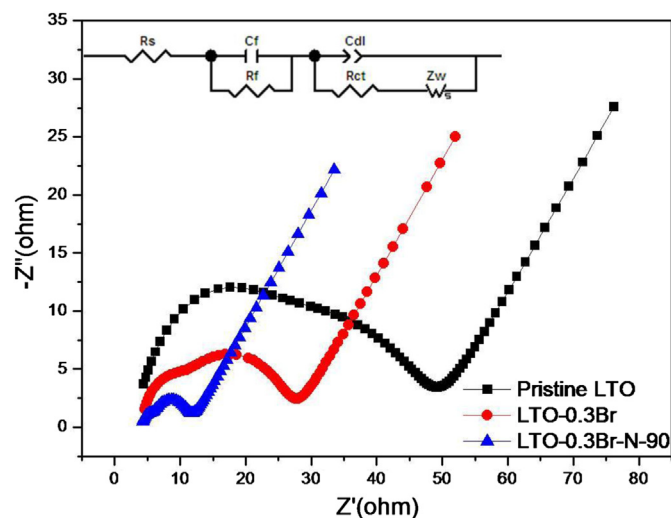


Fig. 9. Nyquist plots of the pristine LTO, LTO–0.3Br and LTO–0.3Br–N-90 samples, as well as the equivalent circuit used to fit the EIS (the inset). The Z' and Z'' represent the real and virtual part of the complex-valued impedance, respectively.

Table 2

The impedance parameters of the derived pristine LTO, LTO–0.3Br and LTO–0.3Br–N-90 electrodes using the equivalent circuit model.

Samples	R_f (Ω)	R_{ct} (Ω)
Pristine LTO	13.2	33.1
LTO–0.3Br	4.8	18.2
LTO–0.3Br–N-90	1.5	5.8

lattice fringe (marked in Fig. 5b) is indexed and calibrated to have a lattice spacing of $d = 4.8$ Å, corresponding to (111) plane of pure LTO, which also confirms that the dopant Br^- replace O^{2-} and enter the crystal lattice of LTO. After calcination in NH_3 for 30 min, the LTO structure remained with a glassy layer (thickness: ~ 1.8 nm) on the surface, as shown in Fig. 5c. In case of nitridation for 90 min, some of the glassy layer became crystalline with a thickness of ~ 4 nm (Fig. 5d). The crystal structure has a lattice spacing of $d = 2.1$ Å, which can be identified as (200) plane of TiN (JCPDS No. 38-1420). The results also show that the longer the nitridation time will lead to the thicker layer that may be composed of Ti and N [1] from the decomposition of LTO–0.3Br.

XPS spectroscopy was conducted to verify the existence of Ti^{3+} . As shown in Fig. 6a & b, typical doublet $\text{Ti}2p$ peaks at 458.3 eV and 464.2 eV appeared in the samples before and after nitridation, associated to characteristic peaks of Ti^{4+} in an octahedral environment. After nitridation, a pair of peaks of new $\text{Ti}2p$ were observed at 457.6 eV and 462.9 eV as shown in Fig. 6b, which may be assigned to the presence of Ti^{3+} [40–42]. The XPS spectrum of C1s peak also displayed some differences between the samples before and after nitridation (Fig. 6c and d). The C1s peak exhibited three components located at 284.8 eV, 286.4 eV and 289.5 eV, respectively. The peak at 284.8 eV corresponds to the C–O bond. The peaks at 286.4 eV and 289.5 eV correspond to C–O bond and a

small quantity of adsorbed species at the surface (COO bond) respectively. After nitridation, the C1s peak exhibited two new components located at 288.6 eV and 290.0 eV which can be assigned to COO bond and OCOO bond respectively, suggesting that LTO has decomposed on the surface of the grain to form Li_2CO_3 . The formation of Ti ion with lower valence proves the occurrence of TiN , in agreement with the EDX (energy dispersive X-ray spectrum) result. Fig. 7 shows the EDX mapping images of the Ti and N elements of LTO–0.3Br–N-90. It can be observed that the distribution of N element is consistent with that of Ti, indicating uniformly distribution of N on the surface of LTO–0.3Br–N-90. Here, the presence of elements Cu and Fe in the spectrum results from the specimen holder (Cu mesh) in TEM.

Fig. 8a compares the rate capabilities of the LTO–0.3Br–N-30, LTO–0.3Br–N-90, and LTO–0.3Br–N-150 with LTO–0.3Br. All the nitridated LTO–0.3Br samples showed better specific capacity than that of LTO–0.3Br, which indicates that the nitridation process could improve the surface electronic conductivity of LTO. The capacity of LTO–0.3Br is slightly lower than those of the other three nitridated LTO–0.3Br samples when cycled at 1C. LTO–0.3Br–N-90 exhibits the highest reversible capacity and best rate capabilities among the three nitridated LTO–0.3Br samples. LTO–0.3Br–N-90 still delivers a capacity of 82 mAh g^{-1} at a high rate of 30C. While for LTO–0.3Br–N-30, it only delivers a capacity of 58 mAh g^{-1} . These results demonstrate that the short time of thermal nitridation cannot form a uniform coating layer, resulting in a discontinuous electronic conducting network (TiN) forming on the surface of LTO–0.3Br [1].

The charge–discharge voltage profiles of LTO–0.3Br–N-90 at different C-rates (from 1C to 20C) are displayed in Fig. 8b. It delivers a reversible capacity of 175 mAh g^{-1} at 1C, which is close to the theoretical capacity of LTO. When the current density increased to 5C, 10C, and 20C, the capacities can be maintained as 167, 138, and

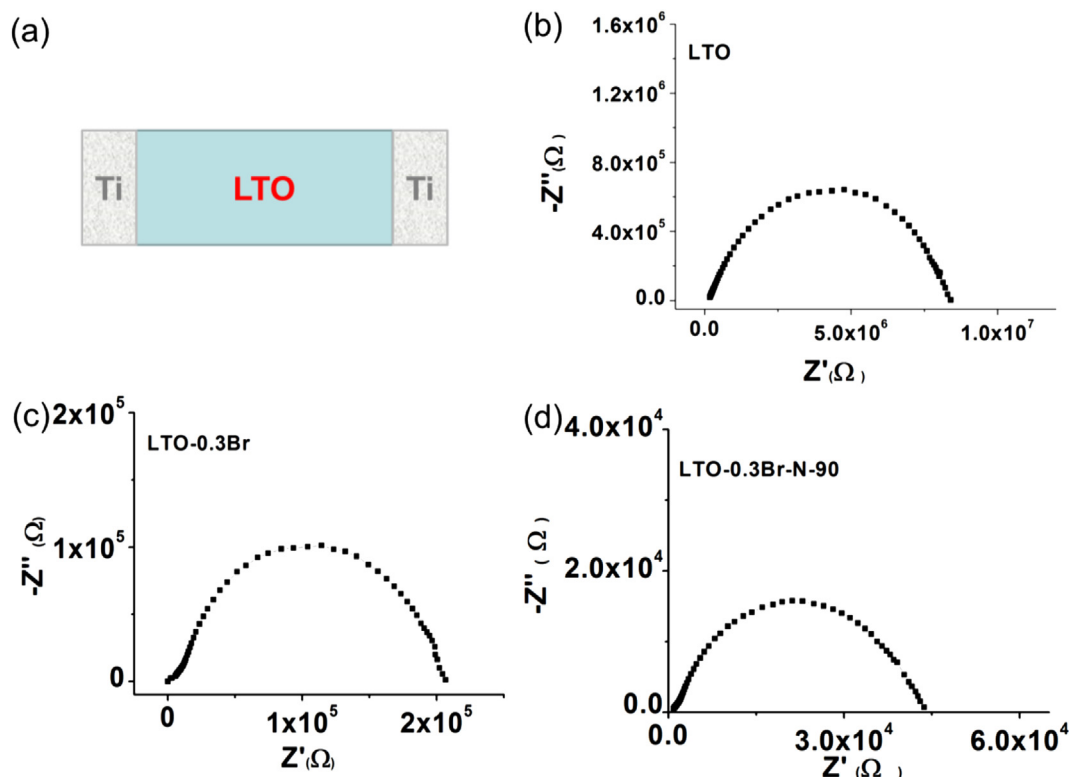


Fig. 10. (a) Schematic picture of ion blocking cell. Nyquist plots of LTO (b), LTO–0.3Br (c) and LTO–0.3Br–N-90(d).

104 mAh g⁻¹, respectively. It implies that modifying the surface structure by thermal nitridation allows for facile transport of both electrons and Li ions.

In order to investigate the effect of TiN layer on the LTO–0.3Br, we plotted the polarization of ΔE versus rate of the LTO–0.3Br and the LTO–0.3Br–N-90 electrodes, respectively (Fig. 8c). The values of ΔE are defined as the differences between the potentials of 50% fully charge and 50% fully discharge plateaus. Both plots showed nearly a linear dependence with relation to the discharge/charge rates, which indicates an ohmic behavior of both electrodes at these C rates. Note that the LTO–0.3Br–N-90 electrode shows lower ΔE value than that of LTO–0.3Br at the same current density, suggesting that the thermal nitridation process decrease the polarization resistance significantly and favor the improvement of the rate capabilities.

The LTO–0.3Br–N-90 electrode also displayed an excellent cycling performance at 10C and 20C, respectively, as shown in Fig. 8d. The reversible capacity is 138 mAh g⁻¹ at 10C after 100 cycles. At a higher current density of 20C, it still delivered a reversible capacity of 104 mAh g⁻¹ after 100 cycles, corresponding 59% of theoretical capacity. These results demonstrate the perfect structure stability of LTO–0.3Br–N-90 and fast electronic and ionic transport in the electrode, which attribute to both surface termination (TiN layer) and bulk doping (Br⁻) of the LTO.

In order to gain insight into the remarkable rate performance of LTO–0.3Br–N-90, AC impedance spectra measurements were carried out. Fig. 9 shows the spectra of LTO, LTO–0.3Br and LTO–0.3Br–N-90 samples, respectively. The inset of Fig. 9 represented the equivalent circuit. There were two semicircles at high-to-intermediate frequency range and a straight line tail in the low frequency region for all samples. An intercept at the Z' real axis in the high frequency represents to the resistance of the electrolytes (R_s) and the semicircle in the high frequency corresponding to R_f is characteristic of the surface film formed on the electrodes. The medium frequency semicircle is characteristic of the charge-transfer resistance (R_{ct}) related to lithium ion interfacial charge transfer. As shown in Table 2, the R_{ct} of LTO–0.3Br–N-90 (5.8 Ω) was much lower than pristine LTO (33.1 Ω) and LTO–0.3Br (18.2 Ω), indicating that thermal nitridation of LTO is an effective strategy to reduce overall electrode ohmic resistance and thus relating to a better rate capability.

To further investigate the electronic conductivity of LTO, LTO–0.3Br and LTO–0.3Br–N-90 samples, symmetric titanium electrodes were used as the ion blocking cell (Fig. 10a). Ti is highly reversible for electrons but not for lithium ions. The total conductivities and the corresponding spectrum are shown in Fig. 10b–d. A nearly semicircle were obtained over the whole frequency range (10^7 – 10^{-2} Hz) at room temperature. The absence of other semicircles or Warburg response demonstrates the absence of blocking grain boundaries and good contact to the electrodes. What's more, the spectra indicate a predominant electronic conductivity. The electronic conductivities for LTO, LTO–0.3Br and LTO–0.3Br–N-90 samples are 7.6×10^{-8} , 3×10^{-6} , and 1.5×10^{-5} S cm⁻¹, respectively. The result validates that both nitridation and Br-doping could effectively improve the electronic conductivity of LTO electrode.

4. Conclusions

In Summary, we have succeeded in synthesizing cubic spinel Li₄Ti₅O_{12-x}Br_x ($0 \leq x \leq 0.4$) and nitridated Br-doped Li₄Ti₅O₁₂. The optimized amount of Br-doping into LTO is $x = 0.3$. The Li₄Ti₅O_{11.7}Br_{0.3} electrode shows enhanced cyclability and delivers a reversible capacity of 167 mAh g⁻¹ after 100 cycles at 0.2C. After 90 min thermal nitridation, LTO–0.3Br–N-90 electrode exhibits

improved rate capability and excellent cycling performance. It still delivers a reversible capacity of 104 mAh g⁻¹ at 20C after 100 cycles, corresponding to 59% of theoretical capacity. This work indicates the feasibility of improving cycling performance and rate capabilities of Li₄Ti₅O₁₂ through both surface termination and bulk doping procedures.

Acknowledgments

This work was financially supported by the National Natural Science Foundation of China (No.21171015, No. 21373195, and No 11174334), the “1000 plan” from Chinese Government, program for New Century Excellent Talents in University (NCET), and the Fundamental Research Funds for the Central Universities (WK2060140014, WK2060140016). L. G. acknowledges the financial support from the “Hundred Talents” program from the Chinese Academy of Sciences.

References

- [1] K.-S. Park, A. Benayad, D.-J. Kang, S.-G. Doo, J. Am. Chem. Soc. 130 (2008) 14930–14931.
- [2] H.F. Xiang, X. Zhang, Q.Y. Jin, C.P. Zhang, C.H. Chen, X.W. Ge, J. Power Sources 183 (2008) 355–360.
- [3] S.S. Zhang, J. Power Sources 161 (2006) 1385–1391.
- [4] A.S. Prakash, P. Manikandan, K. Ramesha, M. Sathiy, J.M. Tarascon, A.K. Shukla, Chem. Mater. 22 (2010) 2857–2863.
- [5] D. Wang, D. Choi, J. Li, Z. Yang, Z. Nie, R. Kou, D. Hu, C. Wang, L.V. Saraf, J. Zhang, I.A. Aksay, J. Liu, ACS Nano 3 (2009) 907–914.
- [6] K. Amine, I. Belharouak, Z. Chen, T. Tran, H. Yumoto, N. Ota, S.-T. Myung, Y.-K. Sun, Adv. Mater. 22 (2010) 3052–3057.
- [7] Y. Wang, H. Liu, K. Wang, H. Eiji, Y. Wang, H. Zhou, J. Mater. Chem. 19 (2009) 6789–6795.
- [8] T. Ohzuku, A. Ueda, Solid State Ionics 69 (1994) 201–211.
- [9] T. Ohzuku, A. Ueda, N. Yamamoto, J. Electrochem. Soc. 142 (1995) 1431–1435.
- [10] K. Zaghib, M. Armand, M. Gauthier, J. Electrochem. Soc. 145 (1998) 3135–3140.
- [11] D. Peramunage, K.M. Abraham, J. Electrochem. Soc. 145 (1998) 2609–2615.
- [12] K. Zaghib, M. Simoneau, M. Armand, M. Gauthier, J. Power Sources 81–82 (1999) 300–305.
- [13] G.G. Amatucci, F. Badway, A. Du Pasquier, T. Zheng, J. Electrochem. Soc. 148 (2001) A930–A939.
- [14] X.L. Yao, S. Xie, H.Q. Nian, C.H. Chen, J. Alloys Compd. 465 (2008) 375–379.
- [15] R. Fong, U. von Sacken, J.R. Dahn, J. Electrochem. Soc. 137 (1990) 2009–2013.
- [16] L. Kavan, J. Rathouský, M. Grätzel, V. Shklover, A. Zukal, J. Phys. Chem. B 104 (2000) 12012–12020.
- [17] C. Jiang, Y. Zhou, I. Honma, T. Kudo, H. Zhou, J. Power Sources 166 (2007) 514–518.
- [18] C.H. Chen, J.T. Vaughey, A.N. Jansen, D.W. Dees, A.J. Kahaian, T. Goacher, M.M. Thackeray, J. Electrochem. Soc. 148 (2001) A102–A104.
- [19] L. Kavan, M. Grätzel, Electrochem. Solid-state Lett. 5 (2002) A39–A42.
- [20] J. Li, Z. Tang, Z. Zhang, Electrochem. Commun. 7 (2005) 894–899.
- [21] L. Shen, X. Zhang, E. Uchaker, C. Yuan, G. Cao, Adv. Energy Mater. 2 (2012) 691–698.
- [22] G.-N. Zhu, H.-J. Liu, J.-H. Zhuang, C.-X. Wang, Y.-G. Wang, Y.-Y. Xia, Energy Environ. Sci. 4 (2011) 4016–4022.
- [23] L. Yu, H.B. Wu, X.W. Lou, Adv. Mater. 25 (2013) 2296–2300.
- [24] E.M. Sorensen, S.J. Barry, H.-K. Jung, J.M. Rondinelli, J.T. Vaughey, K.R. Poeppelmeier, Chem. Mater. 18 (2005) 482–489.
- [25] P. Kubiak, A. Garcia, M. Womes, L. Aldon, J. Olivier-Fourcade, P.-E. Lippens, J.-C. Jumas, J. Power Sources 119–121 (2003) 626–630.
- [26] K. Mukai, K. Ariyoshi, T. Ohzuku, J. Power Sources 146 (2005) 213–216.
- [27] S. Huang, Z. Wen, X. Zhu, Z. Lin, J. Power Sources 165 (2007) 408–412.
- [28] H. Zhao, Y. Li, Z. Zhu, J. Lin, Z. Tian, R. Wang, Electrochim. Acta 53 (2008) 7079–7083.
- [29] Y. Qi, Y. Huang, D. Jia, S.-J. Bao, Z.P. Guo, Electrochim. Acta 54 (2009) 4772–4776.
- [30] Y. Huang, Y. Qi, D. Jia, X. Wang, Z. Guo, W. Cho, J. Solid State Electrochem. 16 (2012) 2011–2016.
- [31] Y. Ma, B. Ding, G. Ji, J.Y. Lee, ACS Nano 7 (2013) 10870–10878.
- [32] H.-K. Kim, S.-M. Bak, K.-B. Kim, Electrochem. Commun. 12 (2010) 1768–1771.
- [33] K. Naoi, S. Ishimoto, Y. Isobe, S. Aoyagi, J. Power Sources 195 (2010) 6250–6254.
- [34] Y. Tang, F. Huang, W. Zhao, Z. Liu, D. Wan, J. Mater. Chem. 22 (2012) 11257–11260.
- [35] Y.-Q. Wang, L. Gu, Y.-G. Guo, H. Li, X.-Q. He, S. Tsukimoto, Y. Ikuhara, L.-J. Wan, J. Am. Chem. Soc. 134 (2012) 7874–7879.
- [36] H. Wu, Y. Huang, D. Jia, Z. Guo, M. Miao, J. Nanopart. Res. 14 (2012) 1–7.

- [37] X. Yang, Y. Huang, X. Wang, D. Jia, W.K. Pang, Z. Guo, X. Tang, *J. Power Sources* 257 (2014) 280–285.
- [38] L. Shen, H. Li, E. Uchaker, X. Zhang, G. Cao, *Nano Lett.* 12 (2012) 5673–5678.
- [39] P.G. Bruce, B. Scrosati, J.-M. Tarascon, *Angew. Chem. Int. Ed.* 47 (2008) 2930–2946.
- [40] J.P. Huang, D.D. Yuan, H.Z. Zhang, Y.L. Cao, G.R. Li, H.X. Yang, X.P. Gao, *RSC Adv.* 3 (2013) 12593.
- [41] X. Lai, Q. Guo, B.K. Min, D.W. Goodman, *Surf. Sci.* 487 (2001) 1–8.
- [42] P. Cheng, M. Zheng, Y. Jin, Q. Huang, M. Gu, *Mater. Lett.* 57 (2003) 2989–2994.